Customized anterior segment photoacoustic imaging for ophthalmic burn evaluation *in vivo*

Huangxuan Zhao[1,2,3†], Ke Li[2,3,4†], Fan Yang[1], Wenhui Zhou[1], Ningbo Chen[2], Liang Song[2], Chuansheng Zheng[1]*, Zhicheng Liu[3,4]* and Chengbo Liu[2]*

Photoacoustic imaging has many advantages in ophthalmic application including high-resolution, requirement of no exogenous contrast agent, and noninvasive acquisition of both morphologic and functional information. However, due to the limited depth of focus of the imaging method and large curvature of the eye, it remains a challenge to obtain high quality vascular image of entire anterior segment. Here, we proposed a new method to achieve high quality imaging of anterior segment. The new method applied a curvature imaging strategy based on only one time scanning, and hence is time efficient and more suitable for ophthalmic imaging compared to previously reported methods using similar strategy. A custom-built photoacoustic imaging system was adapted for ophthalmic application and a customized image processing method was developed to quantitatively analyze both morphologic and functional information in vasculature of the anterior segment. The results showed that the new method improved the image quality of anterior segment significantly compared to that of conventional high resolution photoacoustic imaging. More importantly, we applied the new method to study ophthalmic disease in an *in vivo* mouse model for the first time. The results verified the suitability and advantages of the new method for imaging the entire anterior segment and the numerous potentials of applying it in ophthalmic imaging in future.

Keywords: photoacoustic imaging; ophthalmic imaging; morphologic and functional information; ophthalmic disease; anterior segment

Introduction

The ophthalmic diseases are widespread throughout the world and pose a serious threat to our society[1,2]. Studies have shown that glaucoma, cataract, and many ocular vascular diseases are all serious conditions and should be diagnosed early for a better outcome. All these diseases are characterized by changes in blood microcirculation in the anterior segment of the eye[3–5]. Thus, diagnosing ophthalmic diseases by monitoring blood microcirculation in the anterior segment has gained prominence[3,6,7]. The current imaging techniques used for ophthalmic microcirculation monitoring, including fluorescence imaging (FA) and optical coherence tomography (OCT), are not ideal in application to anterior segment due to several

reasons. The FA method, which needs an injection of external contrast agents, has many limitations: 1) If the size of the injected contrast agent is too small, the agent will leak through vessels. On the other hand, if the size is too large, the imaging result will be dominated by speckles, making it difficult to identify the microvessels. 2) The contrast agent used in FA cannot reach the blocked lesions. 3) The injection of contrast agent is painful to patients, and would cause nausea, vomiting and allergic reactions in almost 10% of the patients[8,9]. The OCT obtains ocular blood vessels images through the Doppler Effect and is used widely in the diagnosis of fundus diseases[10−13]. However, due to the slow blood flow in anterior segment velocity, the image quality using OCT would be suboptimal[14−16].

A new promising biomedical imaging device called optical-resolution photoacoustic microscopy (OR-PAM), which images both anatomical and functional information with high quality[17−20], is now being considered for a variety of ophthalmic diseases[21−26]. A nanosecond pulsed laser is applied to shed laser into the eye. The absorbed laser energy by oxy- and deoxy- hemoglobin in blood vessels of the eye generates acoustic waves through thermoelastic process. The generated acoustic waves (also termed as photoacoustic signals) are captured by an ultrasound transducer outside of the eye to form a photoacoustic image[24,27]. Due to the optical transparency of the eye, the anterior parts of the eye are most optimal for imaging using OR-PAM[23,28,29]. Recently, OR-PAM has been used to evaluate the diseased albino and pigmented animal eyes[15,16,29−33]. However, due to the short depth of focus (DOF) of OR-PAM and large curvature of the anterior segment of the eye, it is difficult to obtain high-quality images of the entire anterior vasculature. Thus, the use of OR-PAM for complete disease assessment in anterior segment is still challenging. To the best of our knowledge, the image quality degradation caused by the curvature of the eyeball has not been well addressed so far in OR-PAM for anterior vasculature imaging and the evaluation of morphologic and functional changes in the eye before and after lesion occurrence has not been performed.

Recently, a new photoacoustic microscopy using contour scanning has been proposed to deal with the challenge of curved surface[34,35]. However, the reported method requires three steps for contour scanning. First, sparse scanning of the sample is performed in a conventional way. After that, curvature of the surface is calculated using the contour extraction algorithm. Finally, the contour is used for fine scanning to obtain high quality image. While this method is efficient in applications such as brain imaging, it has limitation when used for ophthalmic imaging. First, the sample needs to be scanned twice, which is not feasible in living eyeball as the contour of the second scan is highly likely to be different from the first scan due to the movement of the eyeball. Second, the imaging device is complicated for ophthalmic use due to the existence of both mechanical scan for accurate contour acquisition and MEMS scan for fast speed.

In this study, a new ophthalmic photoacoustic microscopy customized for anterior segment imaging has been developed. The microscopy is capable of obtaining high quality image of the anterior segment with a much simpler yet robust contour scanning method compared to the existed one. Only one time scanning is needed during imaging. And a customized vascular quantification algorithm is applied to acquire high quality morphologic and functional images of the vasculature. To evaluate the performance of the new method, the image of a healthy mouse anterior segment was captured and compared with that obtained with traditional OR-PAM. More importantly, to assess the value of the new method in ophthalmic disease applications, *in vivo* anterior segment burn model, which is a regularly seen ocular trauma, was applied to five mice, and the resulted images are analyzed statistically. The detail of the method and *in vivo* studies are presented in the following sections.

Materials and methods

Experimental setup

The ophthalmic photoacoustic microscopy in this study is adapted on a custom-built OR-PAM system reported previously[23,28]. Figs. 1(a) and 1(b) show the schematic of the ophthalmic microscopy and the physical map of a mouse during imaging, respectively. In this system, a 560 nm optical parametric oscillator (OPO) pulsed laser (NT-242, Ekspla, Vilnius, Lithuania) and a 532 nm Nd:YAG pulsed laser (GKNQL-532, Beijing Guoke Laser Co., Beijing, China) were used as the illumination source. Both laser sources have a repetition rate of 1 kHz. The output of the two laser beams are first converged by a dichroic mirror (DM), which reflects the 532 nm light and transmits the 560 nm light, and then reshaped by an iris (ID25SS, Thorlabs, 2 mm aperture size). The
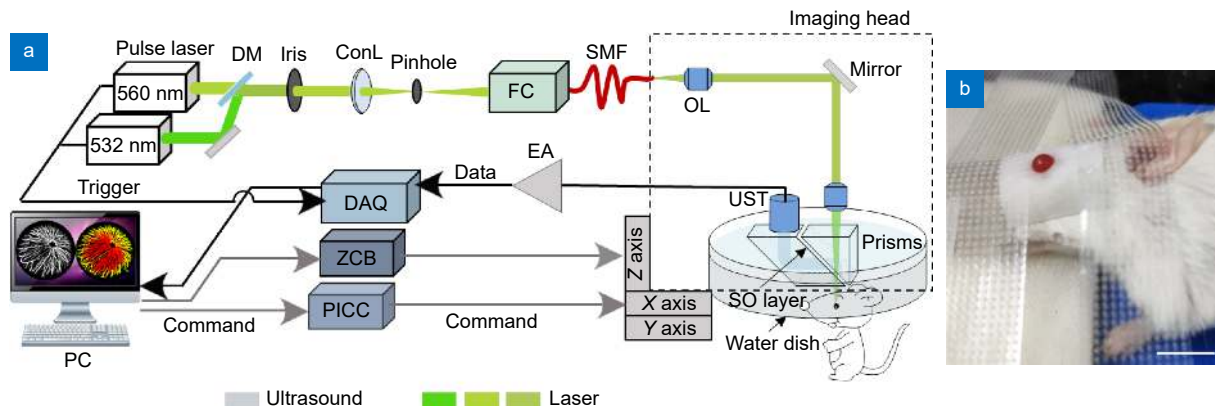
Fig. 1 | (a) The ophthalmic photoacoustic microscopy developed in this study. DM, dichroic mirror; ConL, condenser lens; FC, fiber coupler; SMF, single-mode fiber; OL, objective lens; UST, ultrasonic transducer; SO, silicone oil; EA, electrical amplifier; DAQ, Adata acquisition; ZCB, Zolix control box; PICC, Physik Instrumente control card; PC, personal computer. **(b)** The physical map of a mouse during imaging; Scale bar=10 mm.

reshaped beam gets focused by a condenser lens (LA1131, Thorlabs) before passing through a 50 μm pinhole (P50C, Thorlabs). It is then launched into single-mode fiber (P1-460A-FC-2, Thorlabs) coupled to the fiber coupler (F-91-C1, Newport). The output of the single-mode fiber is first collimated by an objective lens (RMS4X, Thorlabs), and then reflected by a stationary mirror to fill the back aperture of another identical objective lens (imaging objective) to achieve optical focusing. The focused spot is illuminated on the imaging sample to generate photoacoustic signals, which are then collected by a single-element ultrasound transducer (V2022, Olympus-NDT, Kennewick, WA, USA, Center frequency: 50 MHz). The acquired signals are further amplified by an amplifier and then transmitted to the data acquisition card (CS1422, Gage Applied Technologies Inc., Lockport). The imaging head (framed by a black dotted line) of OR-PAM mainly consists of a set of individually designed prisms, a water tank, two objective lenses, a single-element ultrasound transducer and a 3-axis platform (VT-80, Physik Instrumente, Germany). The *x-y* axis is driven by the PI control card (Corvus PCI, Physik Instrumente, Germany), and the *z*-axis is driven by the Zolix control box (SC300, Zolix, China). To achieve contour scanning, the control card and control box work independently but synchronize with each other. For morphologic imaging, the custom-built OR-PAM system has a scanning step size of 2 μm and a spatial resolution of 3.15 μm[31]. The thinnest capillaries in this study have a diameter of ~4 μm, hence the resolution meets the requirement of capillary imaging[36]. For functional imaging, to accurately measure sO_2, an optimum 5 μs trigger delay was applied to the 532 nm laser

compared to the 560 nm OPO laser. This delay is applied to ensure no interference occurs between the photoacoustic signals of the two wavelengths while also ensure minimal change of blood functional will occur due to the delay.

Contour scanning method

We extracted the contour of 30 mouse eyeballs based on their photoacoustic images (as shown in Appendix Fig. A1). The mice are aged from 8–24 weeks and hence they have different size of eyeballs and therefore different contours. Based on a Random Sample Consensus (RANSAC) statistical method[37], five contours were selected and verified to be sufficient to represent all cases. Five eyeball fixation devices (numbered N1–N5) matching each of the contours were designed subsequently and applied to ophthalmic imaging in this study to fix the eye and provide contour information of the eyes. The fixing devices (one design diagram was shown in Fig. 1(b)) were designed by the Solidworks software (SolidWorks Corporation, Massachusetts, USA) and printed by a 3D printer (Form 2, Formlabs, USA). The centers of the fixing devices are drilled with holes to expose the entire anterior segment for imaging purpose.

Animal preparation and imaging

All animal handling and experimental procedures were conducted according to a protocol approved by the Animal Study Committee of Shenzhen Institutes of Advanced Technology, Chinese Academy of Sciences. Five mice numbered No.1 to No.5 were selected for photoacoustic imaging. Among them, the right eyeballs of No.1–No.4 mouse were burned (20 mJ/cm^{2}). The mouse

of NO.5 was not burned and used as control. The mice were placed under an optical microscope (JSZ6D, Jiangnan, China) to observe the changes in eyeballs before and after burns. Photoacoustic imaging was carried out both before and after eye burning. During the imaging, the used laser energy is below 11 mJ/cm^2, which is within the ANSI safety threshold.

During photoacoustic imaging, all mice were remained anesthetized throughout the experiment using 1.5% isoflurane gas (Euthanex, Palmer, Pennsylvania) mixed with oxygen. The right eyelids of the mice were flipped inside out and the eyes were immobilized with the fixing devices and the anterior segments were exposed for imaging. The eyeballs of the mice were placed in an optimal imaging position, i.e., the pupils were faced directly above. However, to verify the robustness of our imaging method, the eyeball of mouse No.4 was placed in a random imaging position by manually rotating the eyeball to make the pupil obliquely faced. To demonstrate the superiority of our method for ophthalmic imaging, one mouse was selected for scanning with both our method and conventional OR-PAM. To confirm that no damage occurred to the eyes during photoacoustic imaging, the mice were euthanized and the imaged eyeballs were removed for histology analysis. The 4% paraformaldehyde was used to fix the eyeball, followed by paraffin-cut sectioning and hematoxylin-eosin (HE) staining to prepare the sample for optical microscopic observation (Axio Lab.A1, ZEISS, Gottingen, Germany).

Vascular morphologic information analysis and functional imaging

The flowchart of vascular morphologic information analysis is shown in Fig. 2(a), and it includes vascular enhancement, extraction, and quantitative analysis of diameter, density, and tortuosity of the vessels. A small region of anterior segment was randomly selected and analyzed before and after burn. The quantitative analysis algorithm was adapted from our earlier publications[23,28]. The work in ref.[23] had excellent performance in vascular enhancement while the work in ref.[28] showed advantages in vascular extraction and quantification. Hence in this study we customized the two algorithms into one algorithm to combine their merits for ophthalmic imaging. Further we replaced exponential transformation with logarithmic transformation in the algorithm to improve vascular extraction efficiency, making it suitable for 3D dataset application.

Vascular enhancement, logarithmic transformation and vascular extraction were performed on the 3D dataset of the anterior segment region to obtain vascularity parameters including vascular diameter, density and tortuosity. The vascular diameter was calculated by extending the vertical direction of the centerline to both sides of the blood vessel wall. The distance was measured once every 10 pixels along the centerline of the blood vessel to
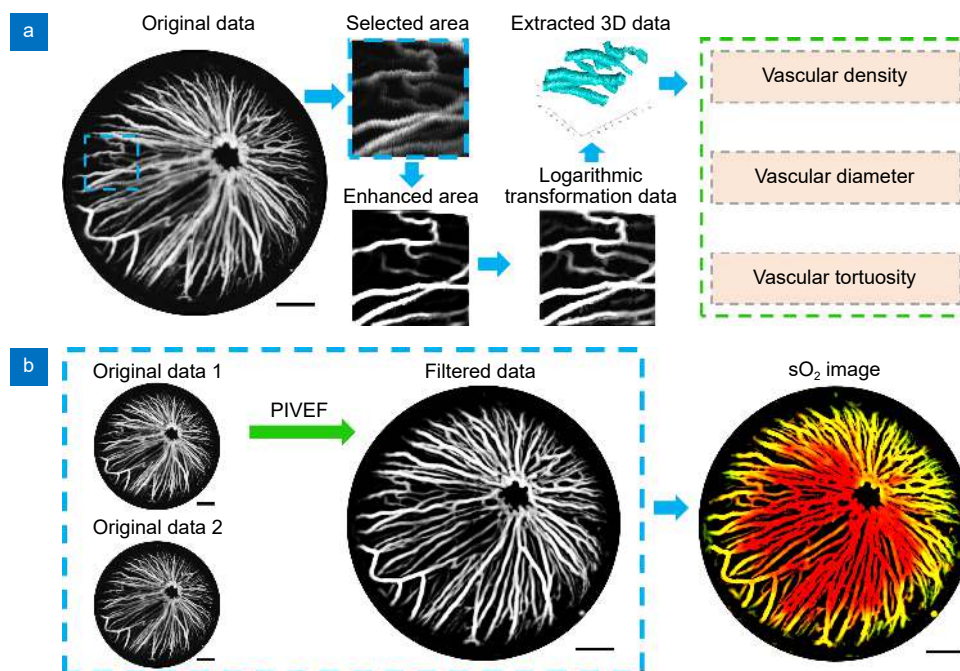

Fig. 2 | (a) The flow chart of vascular morphologic information analysis. **(b)** The flow chart of vascular functional imaging; Scale bar=0.5 mm.

obtain the total diameter. All the measured values were incorporated into a table to draw the diameter distribution histogram. The vascular density is calculated by the ratio of the pixels occupied by the blood vessel to the total number of pixels in the region. For the calculation of vascular tortuosity, three definitions of tortuosity that are widely accepted in the field were used here. Namely, the distance metric (DM), the inflection count metric (ICM), and the sum of angles metric (SOAM). The DM is defined as the ratio between the actual path length of a vessel segment in each subdomain and the linear distance between the two ends of the vessel; the ICM is defined as the ratio between DM and the number of the vessel's inflection points; and the SOAM is defined as the sum of the curvature at all voxels along the centerline of a vessel normalized by the vessel's actual path length[38,39].

After the analysis of vascular morphologic information, functional imaging of anterior segment was performed. The flowchart of vascular functional imaging is shown in Fig. 2(b). More details can be found in ref.[23]. The raw data imaged at 532 nm (Original Data 1) and 560 nm (Original Data 2) is used as input. The Original Data 1 is filtered by Photoacoustic Imaging Vasculature Enhancement Filter (PIVEF) described in our earlier publication[23] to obtain filtered data, which is used as a mask for the sO_2 image (i.e., the morphology basis of the image). The sO_2 was calculated voxel by voxel and the oxygen saturation value of each voxel was filled into the mask to obtain the output sO_2 image.

Results and discussion

Figures 3(a) and 3(b) show the images of a mouse eyeball under optical microscope before and after burn, respectively. From Fig. 3(a), it can be seen that healthy eyeball is transparent, and both blood vessels in iris and the pupil are visible. However, after burn, as shown in Fig. 3(b), the anterior chamber becomes turbid, leading to significant decrease in image quality and hyperemia in the iris. Figure 3(c) shows the HE staining result of a slice of the anterior segment (indicated by the blue dotted line in Fig. 3(a)) after photoacoustic imaging. Both the cornea and iris tissues are normally distributed, indicating no lesions or damages were caused during photoacoustic imaging.

The maximum amplitude projection (MAP) images of a representative mouse scanned by conventional OR-PAM and the ophthalmic photoacoustic microscopy developed in this study are shown in Figs. 4(a) and 4(b), respectively. In Fig. 4(a), except that the blood vessels near
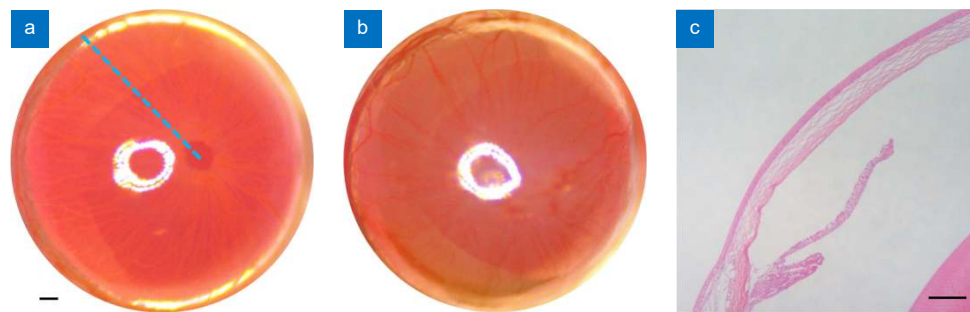

Fig. 3 | (**a−b**) The optical microscopic images of a healthy eyeball before and after burn. (**c**) The HE staining result of the eyeball after photoacoustic imaging. Scale bar=0.2 mm.
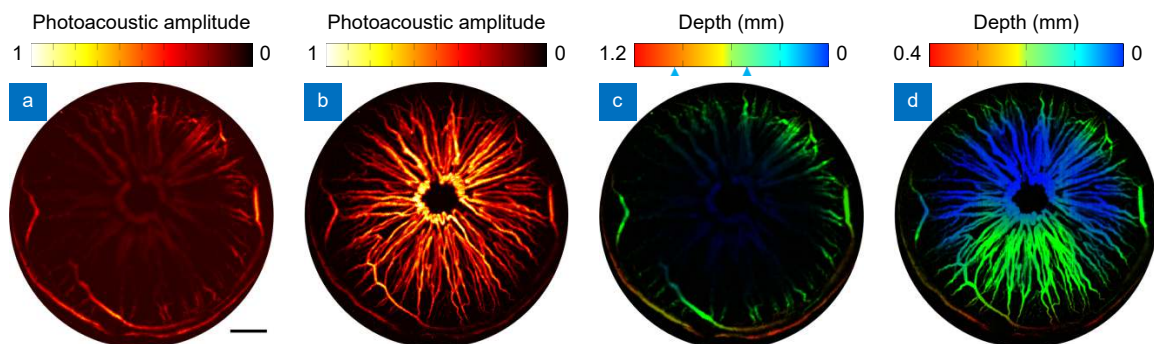

Fig. 4 | (**a−b**) The MAP images of a representative mouse scanned by conventional OR-PAM and the new method developed in this study. (**c−d**). The depth encoded images of (a−b), respectively. Scale bar=0.5 mm.

the DOF of the imaging system show strong photoacoustic signals, the majority of blood vessels in defocused region show weak and fuzzy signals, leading to poor image quality. With the new method, as shown in Fig. 4(b), the entire anterior segment show strong and clear vascular signals and blood vessels of various diameters are visible. Hence the image quality for ophthalmic imaging is significantly improved with our method. To further illustrate the image quality enhancement in the depth direction, the two MAP images in Figs. 4(a) and 4(b) were depth encoded and shown in Figs. 4(c) and 4(d), respectively. The different colors in the images correspond to different depth positions as indicated by the two color bars. From the color bar of Fig. 4(c), it can be seen that the entire vasculature is distributed within a depth range of ~1.2 mm. However, due to the limited depth of focus of conventional OR-PAM, only partial blood vessels were captured in the image. The new method achieves much

higher image quality (Fig. 4(d)) because the curvature scanning enables all the blood vessels within or close to the depth of focus of the imaging system during the imaging process. Correspondingly, the color bar has a depth range of 0.4 mm as shown in Fig. 4(d).

Figure 5 shows the MAP images of all mice in this study (Mouse No.1–No.5) before (first row) and after (second row) burn. Mouse No.5 is the control mouse and no laser burn was applied to it. Hence no significant difference was observed in the control group as shown in Figs. 5(e) and 5(j). Compared to the first row, the blood vessels of the mice (No.1–No.4) after burn are swollen (blood vessels look denser), as shown in the second row. This phenomenon is consistent with previous reports[25,40]. The blood vessels in certain areas vanish after burns, as shown in the red dotted rectangle in Figs. 5(c) and 5(h). To perform more objective analysis, a small region of the imaging area in each mouse (green dotted rectangle) was selected for quantitative analysis and the results are
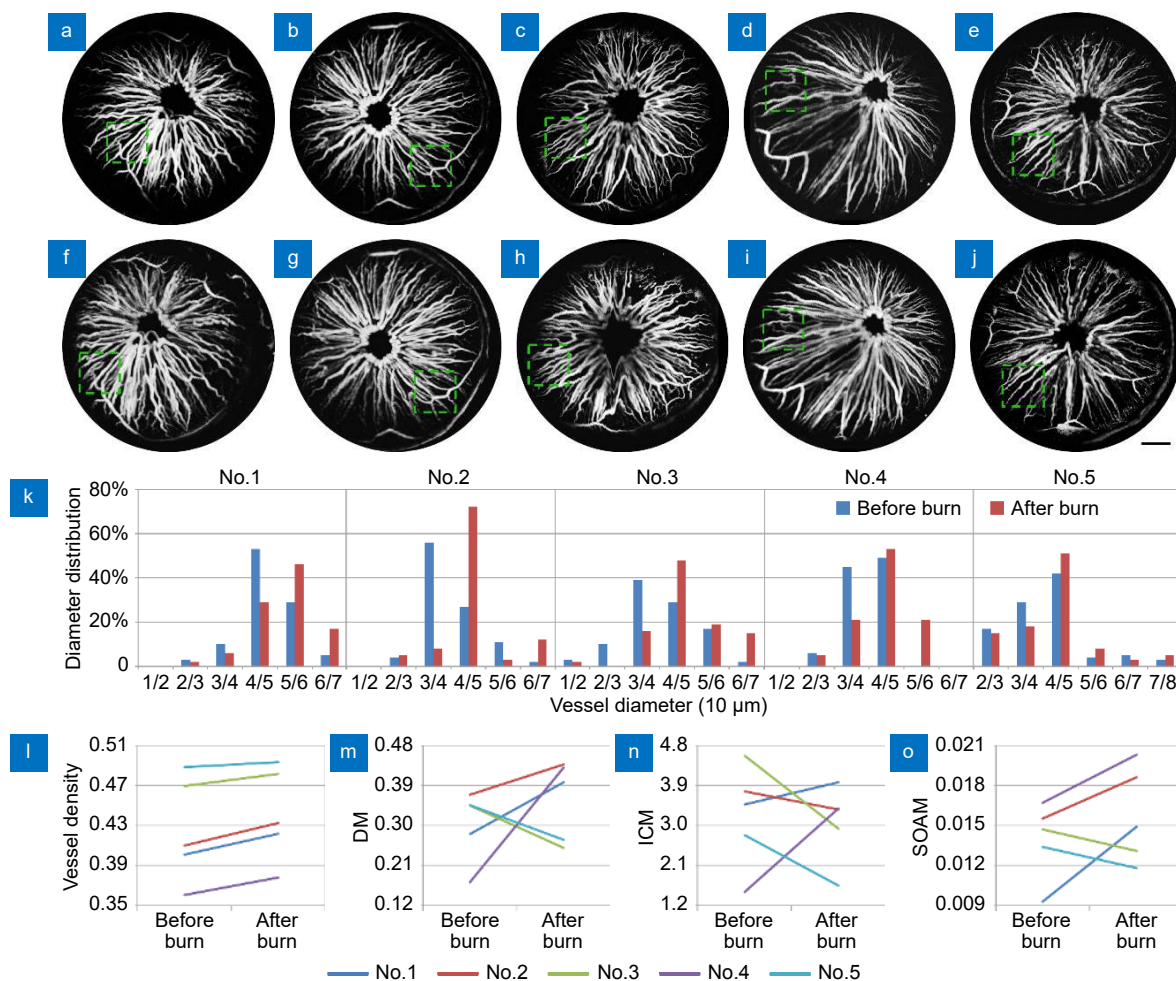

Fig. 5 | (a–j) The MAP images of all mice before and after burn. **(k–o)** Quantitative analysis the vascular information of all mice, including vascular diameter (k), density (l) and tortuosity (m–o). Scale bar=0.5 mm.

shown in Figs. 5(k)–5(o). Figure 5(k) shows the changes of vascular diameter in each mouse. The diameters in Mouse No.1–No.4 have an obvious tendency to increase, i.e. more larger vessels can be seen in the figure. However, in the control group, the increase of diameter is much less significant than other groups. The change of vascular density for each mouse after burn is shown in Fig. 5(l). The vascular density of control group mouse increases much less than that of other mice. The change of vascular tortuosity for each mouse is shown in Figs. 5(m)–5(o), corresponding to the methods of evaluating DM, ICM, and SOAM, respectively. No obvious correlation between tortuosity and burning was found using all three methods, indicating tortuosity may not be a significant parameter for burn assessment. This is presumably due to the fact that tortuosity is affected by multiple factors such as the degree of pupil dilation, blood flow velocity, etc.

The sO_2 maps of Mouse No.1–No.5 before and after burn are shown in Figs. 6(a)–6(e) and Figs. 6(f)–6(j), respectively. The sO_2 values obtained before burns are consistent with the reported literature[41], indicating the accuracy of our method. All burned eyes showed an increasing trend in oxygen saturation. This phenomenon is in line with physiological phenomena, where the exchange of oxygen will be enhanced after burns due to the speed up of sample metabolism. Compared to Mouse No.1–No.4, the oxygen saturation in of the control mouse (Mouse No.5) does not have significant change as show in Figs. 6(e) and 6(j).

Conclusions

The newly developed method dedicated for ophthalmic imaging in this study has several benefits compared to existing methods such as noninvasiveness and high image quality. Compared to conventional OR-PAM, the imaging quality of anterior segment was significantly enhanced in this study, and furthermore, the quantitative analysis of lesions based on vascular information extraction was implemented. Both morphological (density, diameter, and tortuosity) and functional (sO_2) information of blood vessels were extracted and compared before and after lesion inducement.

For pre-clinical and clinical applications, the real time acquisition of images is critical but has posed challenges for imaging systems. At present, the proposed imaging method is based on traditional mechanical scanning, and cannot achieve real-time imaging. However, fast imaging methods have been proposed to meet these challenges[19,42,43].

It was found that the iris blood vessel density and diameter both increased after burn, and the sO_2 value was enhanced. These key findings and indicators may play important role in evaluating the occurrence and development of ophthalmic diseases in the future. Besides that, the new ophthalmic photoacoustic microscopy and imaging method proposed in this study would also enable more opportunities in fundamental research and clinical applications. In the near future, our study has room for improvement: 1. Many new methods have been proposed[44,45], which are expected to be employed in photoacoustic imaging; 2. Various diseases of anterior segment should be studied, and strict statistical rules should be followed to establish exact relationship between degree of lesions and corresponding indicators.
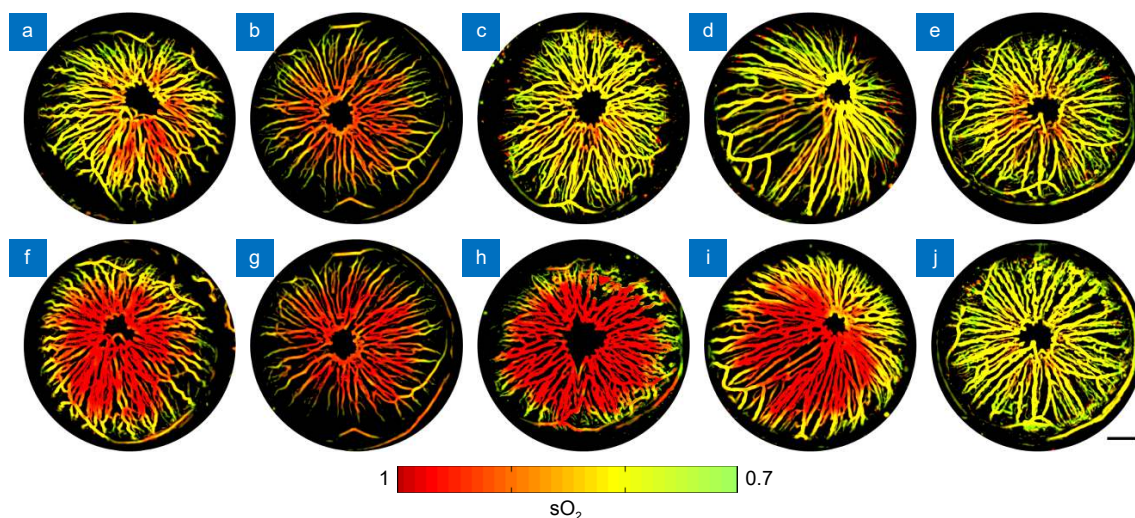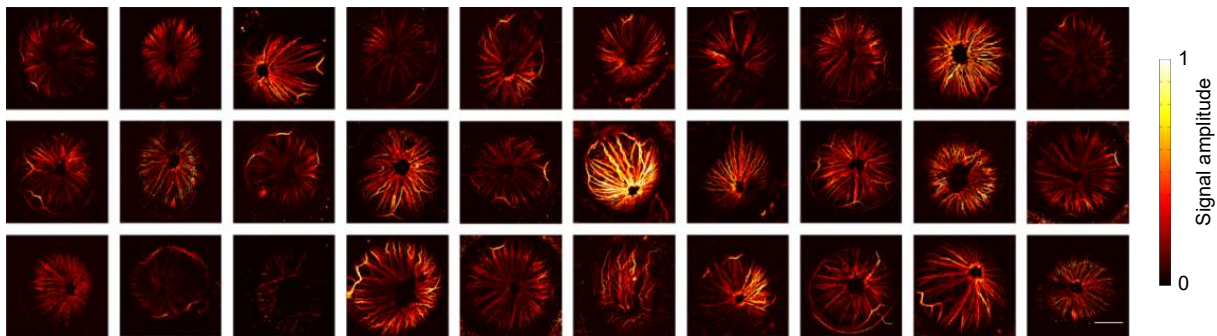

Fig. 6 | The sO$_2$ maps of all mice before and after burn. Scale bar=0.5mm.

Appendix

Appendix Fig. A1 | Photoacoustic imaging results of iris in 30 mice. Scale bar=1 mm.

References

1. Tham YC, Li X, Wong TY, Quigley HA, Aung T et al. Global prevalence of glaucoma and projections of glaucoma burden through 2040: a systematic review and meta-analysis. *Ophthalmology* **121**, 2081–2090 (2014).

2. GBD 2015 Disease and Injury Incidence and Prevalence Collaborators. Global, regional, and national incidence, prevalence, and years lived with disability for 310 diseases and injuries, 1990–2015: a systematic analysis for the Global Burden of Disease Study 2015. *Lancet* **388**, 1545–1602 (2016).

3. Zhang Y, Li SZ, Li L, He MG, Thomas R et al. Dynamic iris changes as a risk factor in primary angle closure disease. *Invest Ophthalmol Vis Sci* **57**, 218–226 (2016).

4. Yang HF, Yu PK, Cringle SJ, Sun XH, Yu DY. Quantitative study of the microvasculature and its endothelial cells in the porcine iris. *Exp Eye Res* **132**, 249–258 (2015).

5. Zhang Y, Li SZ, Li L, He MG, Thomas R et al. Quantitative analysis of iris changes after physiologic and pharmacologic mydriasis in a rural Chinese population. *Invest Ophthalmol Vis Sci* **55**, 4405–4412 (2014).

6. Tan CS, Lim LW, Chow VS, Chay IW, Tan S et al. Optical coherence tomography angiography evaluation of the parafoveal vasculature and its relationship with ocular factors. *Invest Ophthalmol Vis Sci* **57**, OCT224–OCT234 (2016).

7. Ghosh JG, Nguyen AA, Bigelow CE, Poor S, Qiu YB et al. Long-acting protein drugs for the treatment of ocular diseases. *Nat Commun* **8**, 14837 (2017).

8. Dithmar S, Holz FG. *Fluorescence Angiography in Ophthalmology* (Springer, Berlin, 2008).

9. Skalet AH, Li Y, Lu CD, Jia Y, Lee B et al. Optical coherence tomography angiography characteristics of iris melanocytic tumors. *Ophthalmology* **124**, 197–204 (2017).

10. Ong SS, Cummings TJ, Vajzovic L, Mruthyunjaya P, Toth CA. Comparison of optical coherence tomography with fundus photographs, fluorescein angiography, and histopathologic analysis in assessing coats disease. *JAMA Ophthalmol* **137**, 176–183 (2019).

11. Mahmoud H, Eladawi N, Elmogy M, Ghazal M, Alhalabi MT et al. Retinal diseases diagnosis based on optical coherence tomography angiography. In El-Baz AS, Suri JS. *Diabetes and Fundus OCT* (Elsevier, 2020); https://doi.org/10.1016/B978-0-12-817440-1.00006-1.

12. Pellegrini M, Acquistapace A, Oldani M, Cereda MG, Giani A et al. Dark atrophy: an optical coherence tomography an-

giography study. *Ophthalmology* **123**, 1879–1886 (2016).

13. Savastano MC, Lumbroso B, Rispoli M. In vivo characterization of retinal vascularization morphology using optical coherence tomography angiography. *Retina* **35**, 2196–2203 (2015).

14. Choi WJ, Zhi ZW, Wang RK. *In vivo* OCT microangiography of rodent iris. *Opt Lett* **39**, 2455–2458 (2014).

15. Tian C, Zhang W, Mordovanakis A, Wang XD, Paulus YM. Noninvasive chorioretinal imaging in living rabbits using integrated photoacoustic microscopy and optical coherence tomography. *Opt Express* **25**, 15947–15955 (2017).

16. Zhang W, Li YX, Nguyen VP, Huang ZY, Liu ZP et al. High-resolution, in vivo multimodal photoacoustic microscopy, optical coherence tomography, and fluorescence microscopy imaging of rabbit retinal neovascularization. *Light Sci Appl* **7**, 103 (2018).

17. Lai PX, Wang LD, Tay JW, Wang LV. Photoacoustically guided wavefront shaping for enhanced optical focusing in scattering media. *Nat Photonics* **9**, 126–132 (2015).

18. Zhou YY, Cao F, Li HH, Huang XZ, Wei DS et al. Photoacoustic imaging of microenvironmental changes in facial cupping therapy. *Biom Opt Express* **11**, 2394–2401 (2020).

19. Zhou YY, Liang SY, Li MS, Liu CB, Lai PX et al. Optical-resolution photoacoustic microscopy with ultrafast dual-wavelength excitation. *J Biophotonics* **13**, e201960229 (2020).

20. Zhou YY, Chen JB, Liu C, Liu CB, Lai PX et al. Single-shot linear dichroism optical-resolution photoacoustic microscopy. *Photoacoustics* **16**, 100148 (2019).

21. Liu WZ, Schultz KM, Zhang K, Sasman A, Gao FL et al. *In vivo* corneal neovascularization imaging by optical-resolution photoacoustic microscopy. *Photoacoustics* **2**, 81–86 (2014).

22. Liu WZ, Zhang HF. Photoacoustic imaging of the eye: a mini review. *Photoacoustics* **4**, 112–123 (2016).

23. Zhao HX, Li K, Chen NB, Zhang KY, Wang LD et al. Multiscale vascular enhancement filter applied to in vivo morphologic and functional photoacoustic imaging of rat ocular vasculature. *IEEE Photonics J* **11**, 3900912 (2019).

24. Wang LV, Hu S. Photoacoustic tomography: in vivo imaging from organelles to organs. *Science* **335**, 1458–1462 (2012).

25. Jeon S, Song HB, Kim J, Lee BJ, Managuli R et al. *In vivo* photoacoustic imaging of anterior ocular vasculature: a random sample consensus approach. *Sci Rep* **7**, 4318 (2017).

26. Raveendran S, Lim HT, Maekawa T, Matham MV, Kumar DS. Gold nanocages entering into the realm of high-contrast photoacoustic ocular imaging. *Nanoscale* **10**, 13595–13968

(2018).

27. Wang LV, Yao JJ. A practical guide to photoacoustic tomography in the life sciences. *Nat Methods* **13**, 627–638 (2016).

28. Zhao HX, Wang GS, Lin RQ, Gong XJ, Song L et al. Three-dimensional Hessian matrix-based quantitative vascular imaging of rat iris with optical-resolution photoacoustic microscopy in vivo. *J Biomed Opt* **23**, 046006 (2018).

29. Nguyen VP, Li YX, Zhang W, Wang XD, Paulus YM. High-resolution multimodal photoacoustic microscopy and optical coherence tomography image-guided laser induced branch retinal vein occlusion in living rabbits. *Sci Rep* **9**, 10560 (2019).

30. Zhao HX, Chen NB, Li T, Zhang JH, Lin RQ et al. Motion correction in optical resolution photoacoustic microscopy. *IEEE Trans Med Imaging* **38**, 2139–2150 (2019).

31. Zhao HX, Ke ZW, Chen NB, Wang SJ, Li K et al. A new deep learning method for image deblurring in optical microscopic systems. *J Biophotonics* **13**, e201960147 (2020).

32. Lee SW, Kang H, Lee TG. Real-time display and in-vivo optical-resolution photoacoustic microscopy for ophthalmic imaging. *Bioimaging* **2**, 34–38 (2017).

33. Wu N, Ye SQ, Ren QS, Li CH. High-resolution dual-modality photoacoustic ocular imaging. *Opt Lett* **39**, 2451–2454 (2014).

34. Yeh C, Soetikno BT, Hu S, Maslov KI, Wang LV. Microvascular quantification based on contour-scanning photoacoustic microscopy. *J Biomed Opt* **19**, 096011 (2014).

35. Yeh C, Soetikno B, Hu S, Maslov KI, Wang LV. Three‐dimensional arbitrary trajectory scanning photoacoustic microscopy. *J Biophotonics* **8**, 303–308 (2015).

36. Zhou HC, Chen NB, Zhao HX, Yin TH, Zhang JH et al. Optical-resolution photoacoustic microscopy for monitoring vascular normalization during anti-angiogenic therapy. *Photoacoustics* **15**, 100143 (2019).

37. Fischler MA, Bolles RC. Random sample consensus: a paradigm for model fitting with applications to image analysis and automated cartography. *Commun ACM* **24**, 381–395 (1981).

38. Bullitt E, Gerig G, Pizer SM, Lin W, Aylward SR. Measuring tortuosity of the intracerebral vasculature from MRA images. *IEEE Trans Med Imaging* **22**, 1163–1171 (2003).

39. Parikh AH, Smith JK, Ewend MG, Bullitt E. Correlation of MR perfusion imaging and vessel tortuosity parameters in assessment of intracranial neoplasms. *Technol Cancer Res Treat* **3**, 585–590 (2004).

40. Fung SSM, Stewart RMK, Dhallu SK, Sim DA, Keane PA et al. Anterior segment optical coherence tomographic angiography assessment of acute chemical injury. *Am J Ophthalmol* **205**, 165–174 (2019).

41. Hu S, Rao B, Maslov K, Wang LV. Label-free photoacoustic ophthalmic angiography. *Opt Lett* **35**, 1–3 (2010).

42. Yao JJ, Wang LD, Yang JM, Maslov KI, Wong TTW et al. High-speed label-free functional photoacoustic microscopy of mouse brain in action. *Nat Methods* **12**, 407–410 (2015).

43. Zhang C, Zhao HX, Xu S, Chen NB, Li K et al. Multiscale high-speed photoacoustic microscopy based on free-space light transmission and a MEMS scanning mirror. *Opt Lett* **45**, 4312–4315 (2020).

44. Guo JY, Wang T, Quan BG, Zhao H, Gu CZ et al. Polarization multiplexing for double images display. *Opto-Electron Adv* **2**, 180029 (2019).

45. Zhang YB, Liu H, Cheng H, Tian JG, Chen SQ. Multidimensional manipulation of wave fields based on artificial microstructures. *Opto-Electron Adv* **3**, 200002 (2020).

Acknowledgements

Author contributions

H. X. Zhao and K. Li drafted manuscript with equal contribution, C. S. Zheng, Z. C. Liu and C. B. Liu supervised the work and finalized manuscript. All authors commented on the manuscript.

Competing interests

The authors declare no competing financial interests.